Editors' Suggestion

Dissipation engineered directional filter for quantum ratchets

Zlata Fedorova,[1,*] Christoph Dauer,[2,†] Anna Sidorenko,[1,‡] Sebastian Eggert,[2,§] Johann Kroha,[1,‖] and Stefan Linden[1,¶]

[1]*Physikalisches Institut, Rheinische Friedrich-Wilhelms-Universität Bonn, Nussallee 12, 53115 Bonn, Germany*

[2]*Physics Department and Research Center OPTIMAS, Technische Universität Kaiserslautern, 67663 Kaiserslautern, Germany*

(Received 30 October 2020; accepted 17 February 2021; published 19 March 2021)

We demonstrate transport rectification in a Hermitian Hamiltonian quantum ratchet by a dissipative, dynamic impurity. While the bulk of the ratchet supports transport in both directions, the properly designed loss function of the local impurity acts as a direction-dependent filter for the moving states. We analyze this scheme theoretically by making use of Floquet *S*-matrix theory. In addition, we provide direct experimental observation of one-way transmittance in periodically modulated plasmonic waveguide arrays containing a local impurity with engineered losses.

DOI: 10.1103/PhysRevResearch.3.013260

I. INTRODUCTION

Systems governed by time-periodic Hamiltonians can feature a variety of transport phenomena inaccessible in equilibrium. A fascinating example is the ratchet effect, i.e., the ability to convert periodic drive into directed motion without a bias force. The working principle of a ratchet relies on the breaking of space- and time-reversal symmetry which would otherwise not allow a directed current [1]. Introduced by Smoluchowski [2] and Feynman [3], ratchets represent a wide class of microscopic motors, which operate in classical as well as in quantum systems. In particular, the ratchet effect was observed in microbiological [4] and molecular motion [5], semiconductor [6] and superconductor [7] heterostructures, irradiated graphene [8], electron pumps [9], photonic setups [10,11], and Bose-Einstein condensates [12,13].

In most classical ratchets, which are based on thermal motion and dissipation, and in most dissipative quantum ratchets, initial conditions play no role [4,5,14–16]. In contrast, in Hamiltonian quantum ratchets directed transport arises from a quantum coherence effect, namely the Chern number or Berry phase accumulated when a quantum state is moved by the driving potential along a closed loop in Hamiltonian parameter space. When the driving is adiabatic, the transport current is quantized, known as Thouless pumping [17]. The realization of this concept faces, however, two fundamental difficulties. For fast, nonadiabatic driving, the transport quantization generically breaks down, and the transport efficiency depends sensitively on the relative phase of the driving parameters and on the initial state of the driven system [12,13,18–20]. More concretely, being periodic in time, quantum ratchets can be described in terms of Floquet states [18]. The overlap of these states with the initial conditions determines their population and hence their contribution to the current in the stationary state. Since the system's Hamiltonian can support currents in both directions, only a proper choice of the initial conditions will generate maximal, unidirectional transport. In contrast, it is desirable to achieve optimal transport efficiency without initial-state preparation.

In the present study, we propose and experimentally realize a scheme for quantized, directional transport in fast Hamiltonian ratchets using a local impurity with engineered dynamic dissipation as a direction-dependent filter. In the driven Rice-Mele model where space- and time-inversion symmetries are broken by the driven Hamiltonian, any initial condition can carry a current. However, the topological transport quantization is not robust to nonadiabatic effects [21,22] unless intensity or particle losses are introduced globally [20,23]. Since adiabatic conditions cannot be reached in most experimental situations and it is often desirable to minimize losses, we here consider the periodically driven Su-Schrieffer-Heeger (SSH) model. In general, it breaks time-inversion symmetry due to a phase shift between the time-periodic coupling constants, but always preserves space inversion on the Hamiltonian level [11,24–26]. As we will show below, this system supports quantized transport for certain nonadiabatic driving frequencies once the space inversion symmetry is broken by initial conditions. This model and its transport properties are discussed in Sec. II. In Sec. III, we introduce time-dependent losses localized at a finite number of lattice sites (see Fig. 1). Motivated by the conditions of our experimental system, we implement these losses by the imaginary part of the potential. By means of the Floquet formalism, we show how a properly designed, time-periodic local loss function can facilitate nonreciprocal transport through this impurity. In previous studies, local periodic driving of the real part of a potential has been

*cherpakova@physik.uni-bonn.de
†cdauer@physik.uni-kl.de
‡a_sidorenko@uni-bonn.de
§eggert@physik.uni-kl.de
‖kroha@th.physik.uni-bonn.de
¶linden@physik.uni-bonn.de

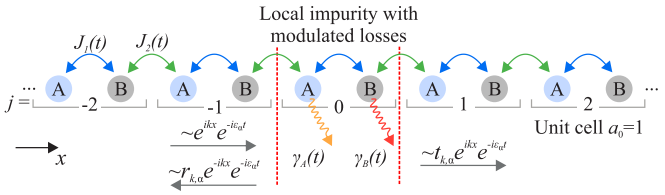

FIG. 1. Sketch of the dimerized tight-binding Floquet chain with local time-periodically modulated decay rates $\gamma_{A/B}(t)$ and hopping amplitudes $J_1(t)$ and $J_2(t)$. We partition the chain in sublattices A/B and label the unit cell by j. The reflection $r_{k,\alpha}$ and transmission $t_{k,\alpha}$ of the Floquet state with quasimomentum k and band index α are schematically indicated by arrows.

used to control transmission through the modulated region [27–29]. In this work, the non-Hermiticity of the impurity is a key feature, as it breaks the relevant space and time-inversion symmetries in the scattering process [20,30,31]. It enables, in combination with the ratchet effect of the driven SSH lattice, the nonreciprocal transport. In Sec. IV, we develop a numerical method based on the Floquet S-matrix theory [32,33] in order to analyze the direction-dependent transmission coefficients in dependence on the system parameters. We find the optimal driving scheme to achieve the largest asymmetry in the transmission for a given decay rate. Furthermore, in Sec. V we provide the experimental observation of transport rectification in arrays of coupled dielectric-loaded surface plasmon-polariton waveguides (DLSPPW) with controlled losses. A brief summary and concluding remarks are given in Sec. VI.

II. RATCHET MODEL

The SSH model [24] consists of a dimerized tight-binding chain with a two-site unit cell and constant, homogeneous onsite potentials (sublattice A has odd sites and sublattice B has even sites; see Fig. 1). Its Hamiltonian is given by

$$H_{\mathrm{Bulk}}(t) = \sum_j J_1(t) c^\dagger_{j,\mathrm{A}} c_{j,\mathrm{B}} + J_2(t) c^\dagger_{j,\mathrm{B}} c_{j+1,\mathrm{A}} + \mathrm{H.c.} \quad (1)$$

Here, $c^\dagger_{j,\mathrm{A/B}}$ ($c_{j,\mathrm{A/B}}$) are creation (annihilation) operators for site A (B) in unit cell j. The time-periodic intra- and intercell coupling constants $J_{1/2}(t)$ are modulated such that $J_1(t) > J_2(t)$ holds for the first half of the period while the situation is inverted in the second half. In this case, the movement of a right-moving excitation from A to B sites in the first half of the period and then from B to A sites can be supported at the special group velocity of one unit cell per driving period and we find that the transport may become largely independent of the magnitude of the quasimomentum. In the experiments below, we sinusoidally vary the spacing between the neighboring sites, which leads to the following functional form of the coupling constants:

$$J_1(t) = J_0 e^{-\lambda(1-\sin(\omega t))}, \quad (2a)$$

$$J_2(t) = J_1(t - T/2). \quad (2b)$$

Here, $\omega = 2\pi/T$ is the driving frequency and T is the period of modulation. To be consistent with the experiment, we choose in the following $\lambda = 2.11$. For simplicity, we measure

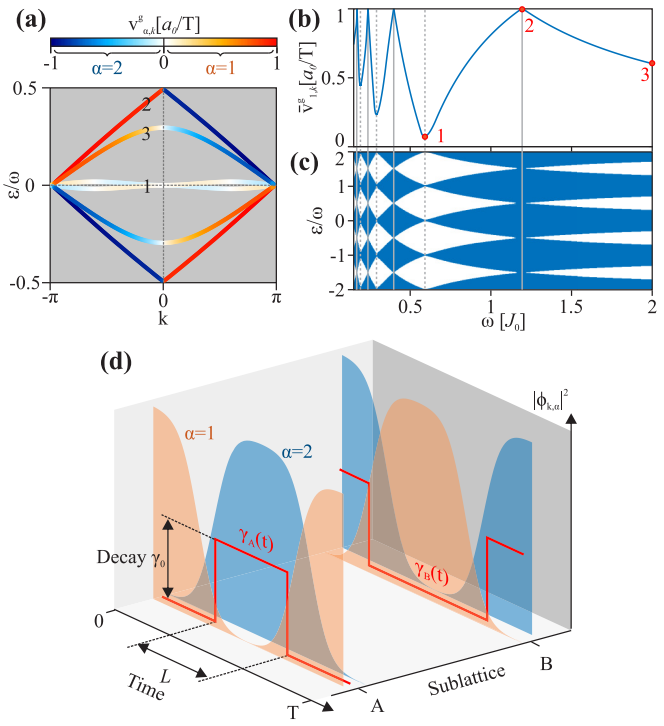

FIG. 2. (a) Band structure in the first FBBZ at three different driving frequencies: 1, $\omega = 0.597J_0$; 2, $\omega = 1.195J_0$; and 3, $\omega = 2J_0$. The color code shows the corresponding group velocity $v^g_{\alpha,k}$. (b) Average absolute value of the group velocity as a function of ω. Gray lines mark values from Eqs. (3) and (4) and numbers highlight the frequencies from panel (a). (c) Quasienergy spectra in dependence on the driving frequency. (d) Squared absolute value of the state amplitude at $\omega = 1.195J_0$ with positive ($\alpha = 1$) and negative ($\alpha = 2$) group velocities along one period at sublattices A and B. Red lines show the time-dependent losses $\gamma_{A/B}(t)$ on sublattices A and B for $\varphi = 0$ which consist of temporal intervals L of the constant decay rate γ_0. Note that in our model $\gamma_{A/B}(t)$ are applied only to the central unit cell as illustrated in Fig. 1.

all the quantities in units of J_0 and set the unit cell as well as the reduced Planck constant to one: $a_0 = 1$ and $\hbar = 1$. The calculation of the bulk quasienergy spectrum is carried out using the Floquet-Bloch theory [34] (see Appendix A) and exemplified in Fig. 2(a) in the first Floquet-Bloch Brillouin zone (FBBZ) for three different ω values. The figure shows that the driving frequency has a huge impact on the band shape: At $\omega = 1.195J_0$ (num. 2) the bands are almost linear with the slope $1/T$; in contrast, at $\omega = 0.597$ (num. 1) they become almost flat. Note that the almost linear, gapless bands are helical in the Floquet-Bloch Brillioin zone and can be related to a nontrivial topology [26]. The chiral symmetry of the Hamiltonian (1) guarantees that the spectrum is always symmetric with respect to the Floquet quasienergy $\epsilon \to -\epsilon$. We can therefore choose to label the quasienergies and the corresponding Floquet-Bloch states according to the sign of the group velocity such that $\alpha = 1$ stands for $v^g \geqslant 0$ while $\alpha = 2$ for $v^g \leqslant 0$. As shown in Fig. 2(b), the group velocity averaged over all ($\alpha = 1$) states, $\frac{1}{2\pi}\int_{-\pi}^{\pi} dk v^g_{1,k}$, depends oscillatory on ω. The quasienergy spectrum in Fig. 2(c) reveals that such a behavior is directly connected to the oscillating size

of the band gap. The ratchet transport is most efficient when the average group velocity reaches its maximum of one unit cell per driving period. These points correspond to gapless helical bands, which in turn possess minimal dispersion. Such a dynamics can be qualitatively understood with a simplified dimer model, which is discussed in Appendix B. There we find that the helical bands and maximum group velocity occur if the states undergo half-cycles of Rabi oscillations between the two sublattices. This physics can be linked to the condition for the velocity maxima and gap closings in terms of the time-integrated hopping

$$\omega_n = \frac{4\int_0^1 d\xi J_i(2\pi/\omega\xi)}{1+2n}, \quad n \in \mathbb{N}_0,\ i = 1, 2. \tag{3}$$

Both hopping constants (2) have the same time average, for which an explicit expression is found by $\int_0^1 d\xi J_l(2\pi/\omega\xi) = J_0 e^{-\lambda}\mathcal{J}_0(i\lambda)$, $l = 1, 2$, where $\mathcal{J}_n(x)$ is the Bessel function of the first kind. Likewise, minima of the group velocity and the bandwidth are predicted to occur near

$$\omega_n' = \frac{4\int_0^1 d\xi J_i(2\pi/\omega\xi)}{2+2n}, \quad n \in \mathbb{N}_0,\ i = 1, 2, \tag{4}$$

where the transport is partially blocked. In Figs. 2(b) and 2(c), it is shown that this correctly predicts extrema of the average group velocity and the closing of the bulk gap in our system. We note that for frequencies larger than ω_0, the energy splitting between the Floquet-Bloch bands becomes larger than the bandwidth. Thus, the coupling between the bands can be neglected and our model behaves like a static tight-binding lattice with one effective hopping constant $J_{\text{eff}} = \int_0^1 d\xi J_i(2\pi/\omega\xi)$, $i = 1, 2$. Here transport is ballistic and no ratchet effect occurs.

In the context of our experimental setup, the achievable frequency range is roughly $\omega \in [0.7J_0; 2J_0]$. Further, we will focus only on the first maximum $\omega_0 = 1.195J_0$ as it lies in this range. The dynamics of the periodic Floquet-Bloch states in this regime is governed by oscillations between the two sublattices [see Fig. 2(d)]: The density of a right-moving state ($\alpha = 1$) tunnels from sublattice A at $t = Tm$ to sublattice B at $t = T/2 + Tm$, while it is fully transferred back at $t = T(m+1)$, where m is an integer. Time-reversal symmetry is present in our model due to the special phase relation between the time-periodic coupling constants (2). This symmetry implies that the aforementioned process is exactly inverted for the left-moving state with the same quasienergy. The ratchet effect occurs when the asymmetric initial conditions are applied at $t = 0$; i.e., the system is initiated at one sublattice A or B. Via Fourier analysis, this results in predominant population of only the left- or right-moving states, respectively. Thus, such an SSH-based ratchet strongly depends on the initial conditions, in contrast to Thouless pumping, where transport is induced by the phase relation between the on-site energies and the coupling constants.

III. DIRECTION-DEPENDENT FILTER

Now, we additionally subject two central lattice sites, A and B, from unit cell $j = 0$, to time-periodic losses oscillating at the same frequency ω as the bulk (see Fig. 1). Losses in the waveguide experiments below are well described by the complex on-site potentials [35,36], so we introduce them as a simple but nontrivial model for the dissipative part. The corresponding Hamiltonian is the sum of the bulk Hamiltonian and the local impurity $V(t)$:

$$H(t) = H_{\text{Bulk}}(t) + V(t), \tag{5a}$$

$$V(t) = -i\gamma_{\text{A}}(t)c_{0,\text{A}}^\dagger c_{0,\text{A}} - i\gamma_{\text{B}}(t)c_{0,\text{B}}^\dagger c_{0,\text{B}}. \tag{5b}$$

The decay rates on sublattices A and B are denoted by $\gamma_{\text{A/B}}(t)$ and have a form of T-periodic step functions; i.e., the onsite losses can be turned on and off in a periodic manner as realized in our experiments below. The mathematical description is given by

$$\gamma_{\text{A}}(t) = \gamma_0 \times \Theta(-\cos(\omega t + \varphi) - \cos(\pi L/T)), \tag{6a}$$

$$\gamma_{\text{B}}(t) = \gamma_{\text{A}}(t - T/2), \tag{6b}$$

where $\Theta(x)$ is the Heaviside function, γ_0 is the loss amplitude, L is the duration of the losses within one period T ($L < T$), and φ is the phase shift. Note that for $\varphi = 0$ the losses are out of phase with the coupling constants; i.e., they are centered at $t = (m + 1/2)T$ on sublattice A and at $t = mT$ on sublattice B.

In the following, we aim at analyzing the scattering process of a quantum particle propagating along the driven SSH chain and scattered by this impurity (see gray arrows in Fig. 1). Assume that the system is driven with the resonant frequency ω_0, so that the bands are helical and the band-averaged group velocity is maximal. In order to understand the origin of nonreciprocal transmission induced by $V(t)$, it is central to look at the periodic exchange of the state density between the two sublattices. In the previous section, it was shown that the counterpropagating Floquet-Bloch states have different spatiotemporal distributions which enabled populating only states moving in the chosen direction by proper choice of the initial conditions. The same feature can be employed for direction-dependent filtering. In particular, when we introduce strong losses at space-time moments, where the maxima of $|\phi_{k,\alpha=2,m}(t)|^2$ reside, the time-reversal symmetry and the oscillatory motion of the states guarantees that $|\phi_{k,\alpha=1,m}(t)|^2$ is minimal at these moments [see red lines in Fig. 2(d)]. Thus, we can effectively absorb only the states moving in the $-x$ direction ($\alpha = 2$ states). The transmission through the impurity can be controlled by tuning such system parameters as γ_0, L, and φ. It is to be expected that with increasing loss strength γ_0 and duration of the losses L transmission in $-x$ direction decreases. But how strongly will the states moving in the opposite direction be affected? What is the influence of the phase shift φ? Does one-way transmission persist at frequencies away from resonance? To answer these questions and to predict optimal parameters for the experiment, we apply Floquet S-matrix theory.

IV. FLOQUET S-MATRIX ANALYSIS

We calculate transmission and reflection coefficients for scattering by the impurity with the use of Floquet S-matrix theory (see Appendix C). As a natural initial condition for the ratchet, we assume a uniform superposition of either all the right- or left-moving states and consider band-averaged

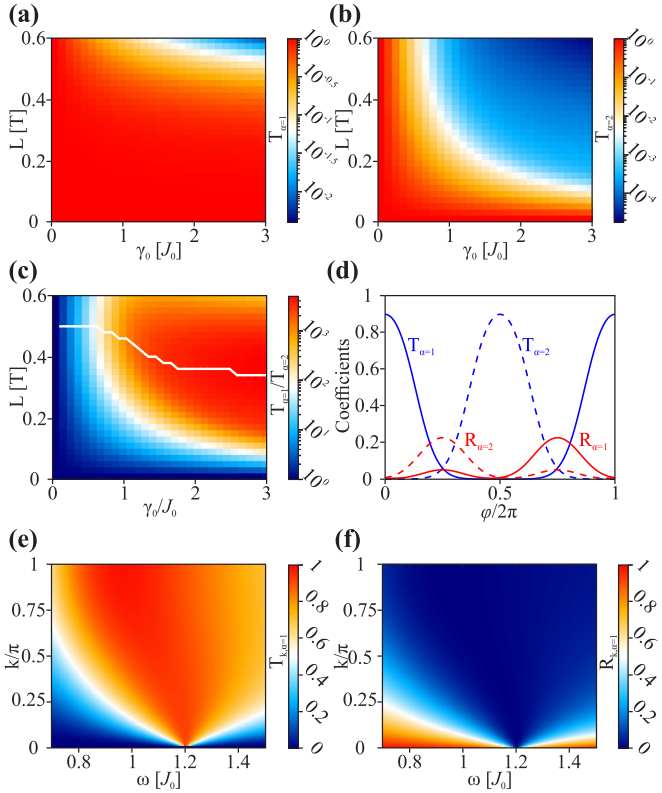

FIG. 3. Transmission of (a) right and (b) left movers over the impurity parameters γ_0 and L at $\omega_0 = 1.195 J_0$. (c) Decadic logarithm of $T_{\alpha=1}/T_{\alpha=2}$ for $\omega_0 = 1.195 J_0$; white line marks the function $\max_L(T_{\alpha=1}/T_{\alpha=2})(\gamma_0)$. (d) Transmission (blue) and reflection (red) of right (solid) of left (dashed) moving states over the shift angle φ for $\gamma_0 = 1.5 J_0$ and $L = 0.25\,T$. (e) Transmission and (f) reflection of right movers for $L = 0.25\,T$ and $\gamma_0 = 1.5 J_0$ over driving frequency ω and quasimomentum k.

quantities [Appendix C, Eq. (C4)]. Figures 3(a) and 3(b) display the transmission over the loss duration L and strength γ_0 at $\varphi = 0$ for the $\alpha = 1$ and $\alpha = 2$ states, respectively. We clearly see that for a wide range of system parameters our proposed scheme works as an excellent direction-dependent filter. This is prominently visible for $L \leqslant 0.5\,T$ where the right-moving states are transmitted with $T_{\alpha=1} = \mathcal{O}(1)$, while the transmission of the left movers drops sharply with increasing γ_0 and L. Similar results are found in the disconnected dimer model in Appendix B, Eq. (B6). The ratio $T_{\alpha=1}/T_{\alpha=2}$ [Fig. 3(c)] quantifies this effect and can exceed 10^3 in the examined parameter range. Our illustrative picture of generating directional losses can be formalized by looking at the matrix elements of the impurity operator in the basis of the Floquet-Bloch states $V_{(q,\beta,n),(k,\alpha,m)} = 1/T \int_0^T dt\, \langle \phi_{q,\beta,n}(t)|V(t)|\phi_{k,\alpha,m}(t)\rangle$, where the states $|\phi_{k,\alpha,m}(t)\rangle$ are calculated by (A4). The parts diagonal in the band index $\alpha, \beta = 1, 2$ determine the size of the transmission, while the off-diagonal ones couple the channels and induce reflection. Evaluating these integrals in our situation shows that the matrix elements for the right movers $V_{(q,1,n),(k,1,m)}$ and the interband coupling $V_{(q,1,n),(k,2,m)}$ are much smaller than for the left movers $V_{(q,2,n),(k,2,m)}$. This leads to the large suppression of the transmission of the left-moving states while the right movers are almost unaffected. Using this picture explains the naively unexpected effect that the ratio $T_{\alpha=1}/T_{\alpha=2}$ has for all γ_0 a maximum at finite L: For small L, the dissipation of both directions is small, leading to $T_{\alpha=1}/T_{\alpha=2} = \mathcal{O}(1)$. At large L, however, especially if $L > 0.5\,T$, also the right movers are strongly damped, which implies a decrease of $T_{\alpha=1}/T_{\alpha=2}$. Here the time interval with losses is so long that they do not fit with the sublattice oscillation of the right movers, leading to larger matrix elements and stronger damping.

We are interested in what happens if the parameters are tuned away from our proposed driving scheme and begin with changing the parameter φ. The resulting transmission and reflection coefficients are shown in Fig. 3(d). At the points $\varphi = 0, \pi$ unidirectional transport is most favorable, as the dissipation peaks such that it only damps either left or right movers strongly. For intermediate values of φ, the losses are present during the intermediate part of the motion of the states [see Fig. 2(d)], where both sublattices host population of substantial weight. This results in a lower ratio $T_{\alpha=1}/T_{\alpha=2}$ compared to $\varphi = 0, \pi$ and confirms that we indeed took the optimal values for our proposed driving scheme. The reflection coefficients have a maximum at $\varphi = \pi/2, 3\pi/2$. Here, the dissipation is centered at the time, when both sublattices are populated equally, creating the largest matrix elements $V_{(q,\alpha,n),(k,\beta\neq\alpha,m)}$ and strongest coupling between the channels. Remarkably, the reflection coefficients are not mirror symmetric about $\varphi = \pi$. We sketch this interesting feature for the case $\varphi = \pi/2$. Here the dissipation is timed such that a wave packet consisting of right-moving states is damped before it performs the sublattice oscillation inside the dissipative region, leading to small reflection. In the case of a left-moving packet, the dissipation is timed such that it delays the sublattice oscillation when the packet is about to enter the lossy region. As a result, a major portion stays outside and thus gets reflected. For $\gamma_0 \to \infty$ and $L \approx 0.5\,T$, this effect increases up to $R_{\alpha=2} \approx 1$ and $R_{\alpha=1} \approx 0$.

In Figs. 3(e) and 3(f), the transmission and reflection coefficients of the right movers are plotted in dependence of quasimomentum k and frequency ω. As the coefficients are symmetric in k, we restrict ourselves to half the Brillouin zone, i.e., $k > 0$. The transmission is $\mathcal{O}(1)$ and homogeneous for all quasimomenta at the point of helical bands $\omega = \omega_0 = 1.1948\,J_0$. Moving away from the ideal case, transmission around $k = 0$ decreases due to hybridization of the quasienergy bands [see Fig. 1(b)], which mixes right- and left-moving states. These hybridized states do not perform a full oscillation between the sublattices, so both right and left movers are affected by the dissipation. This leads to a reduced transmission coefficient in comparison to the ideal case of helical bands. The reflection coefficient shown in Fig. 3(f) is small and homogeneous for $\omega = \omega_0$, while it increases around $k = 0$ due to the fact that the hybridized states lead to a finite interband coupling $V_{(q,\alpha,n),(k,\beta\neq\alpha,m)}$. In the motion of a wave packet, the states near $k = 0$ are slow compared to others as the group velocity tends to zero at $k = 0$. As these parts of the packet reach the impurity at a late time in an experimental setting, our scheme filters out the slow parts in the transmitted packet.

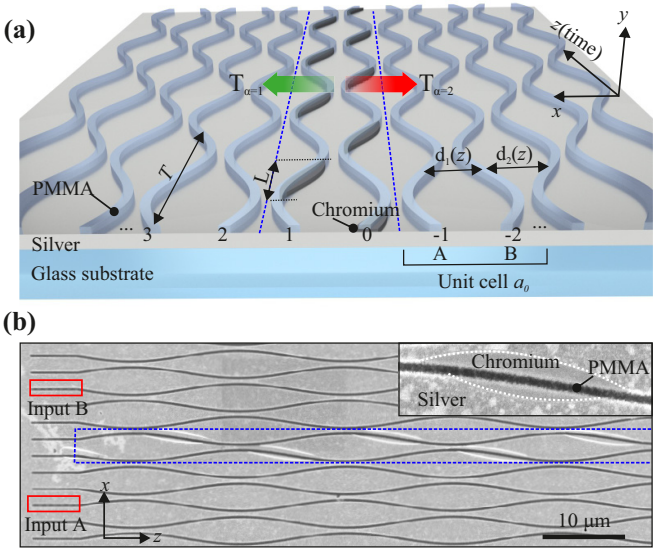

FIG. 4. (a) Sketch of a plasmonic waveguide array featuring unidirectional transmittance. Green and red arrows indicate the low- and high-loss directions, respectively. (b) SEM scan of a typical sample. Inputs A and B are marked by red boxes and blue dotted lines to highlight the region with periodic dissipation. The chromium stripe used to implement losses is magnified in the top right corner.

V. EXPERIMENTS

We realize unidirectional transmittance in arrays of coupled dielectric-loaded surface plasmon polariton waveguides (DLSPPWs). Here, we rely on the mathematical analogy between the tight-binding Schrödinger equation and the paraxial Helmholtz equation, which describes propagation of light in coupled waveguides [37–39]. According to this analogy, time is directly mapped into propagation distance which enables us to mimic a Floquet system by periodic modulation of the corresponding parameters along the waveguide axis [40,41]. Precise control of the system's parameters including losses as well as powerful detection techniques make DLSPPWs an ideal system to investigate transmission through a region with local dynamic dissipation.

A sketch and a scanning electron micrograph (SEM) of a typical sample are shown in Figs. 4(a) and 4(b), respectively. See Appendix D for sample fabrication and geometrical parameters of DLSPPWs. The array displayed in Fig. 4(a) is analogous to a one-dimensional Floquet chain with two sites (waveguides) per unit cell, A and B. The sinusoidal modulation of the center-to-center distances $d_{1,2}(z)$ results in periodic modulation of the corresponding coupling constants. This modulation can be expressed by Eq. (2) since the mode overlap decays as $\propto e^{-ad}$ with the distance d between the waveguides. The parameters from Eq. (2) were determined in an auxiliary experiment with just two waveguides by measuring the coupling length $L_{\text{couple}} = \frac{2\pi}{C}$ in dependence on the distance between two waveguides d. Fitting the function $\ln C(d)$ by a line, we obtain $\lambda = 2.11 \pm 0.21$ and $J_0 = 0.16 \pm 0.05\,\mu\text{m}^{-1}$. Due to strong confinement of SPPs, we can neglect the variation of a propagation constant caused by waveguide bending and consider the real part of the on-site potential to be zero [41]. We introduce local periodic dissipation by deposition of chromium stripes below the waveguides. Cr can cause strong losses with negligible effect on the real part of the effective refractive index [36]. Using simulations based on finite-element analysis (COMSOL MULTIPHYSICS), we estimate the minimum loss strength induced by the Cr layer to be $\gamma_0 = 0.25\,\mu\text{m}^{-1}$. The width of the Cr stripe is designed to be much larger than the width of a waveguide [see Fig. 4(b)]. We can therefore assume the losses to be approximately constant along the whole length of the stripe L as given by Eq. (6). We note that in addition to the engineered losses, the propagation of SPPs is accompanied by the constant decay rate $\beta'' = (7.3 \pm 0.02) \times 10^{-3}\,\mu\text{m}^{-1} \ll \gamma_0$ caused by ohmic losses in the metal, imperfections of the fabricated film, and leakage radiation into the substrate. These losses are assumed to be homogeneous and independent of z. The propagation of SPPs in the array is monitored by real- and Fourier space leakage radiation microscopy (see Appendix E).

First, we consider the case without engineered losses and determine the driving frequency $\omega = 2\pi/T$ at which we can achieve directed transverse motion of SSPs with the highest group velocity v_g. Theory predicts for this case the absence of hybridization of the counterpropagating states and therefore the most pronounced one-way transmission effect. To find the group velocity maximum, we fabricate arrays of modulated DLSPPWs (no Cr is deposited) with various frequencies of modulation. For every array, we measure the real-space intensity distribution $I(x, z)$ (analogous to $|\Psi(x, t)|^2$) after the single-site excitation at the sublattice A. Note that the corresponding data for the input B is just mirrored about $x = 0$. We use the experimental data to extract the position of the center of mass (c.m.) of the wave packet $\langle x\rangle(z) = \sum_j I(x_j, z) \times x_j / \sum_j I(x_j, z)$ as a function of z. The group velocity v_g is found as the slope of the linear fit to $\langle x\rangle(z)$ and plotted in units of a unit cell per driving period a_0/T against ω in Fig. 5(a). The resulting curve reaches the peak value of about 0.63 at $\omega = \Omega_1 \approx 0.23\,\mu\text{m}^{-1}$. We note that the measured peak value of the group velocity is smaller than 1, as would be expected from the completely filled band [see Fig. 2(c)]. We attribute this deviation to the contribution of camera noise and nonperfect excitation conditions. By the latter, we mean that first the overlap of the states moving in the $-x$ direction with the initial conditions is not exactly zero, and second, when guided SPPs are excited by shining laser light onto the grating coupler, the laser spot slightly excites the neighboring waveguides. These factors inevitably decrease the c.m. displacement. The quantitative comparison with the theoretical value of ω_0 in Eq. (3) requires the value of J_0, which has an experimental uncertainty $1.09J_0 \lesssim \Omega_1 \lesssim 2.09J_0$ that is fully consistent with the theoretical value of $\omega_0 = 1.195J_0$. In Figs. 5(b) and 5(c), we compare the real- and Fourier-space intensity distributions for two frequencies Ω_1 (close to the resonance ω_0) and Ω_2 (maximum frequency in our measurements, away from the resonance). In real space, at Ω_1 we observe that the wave packet is confined, and the intensity maximum is transported in positive x direction [Fig. 5(b), top]. The corresponding Fourier intensity distribution $I(k_x, k_z)$ shown in Fig. 5(c) (top) reveals nearly linear dispersion and predominant population of the Floquet states with $v^g_{\alpha,k} > 0$. In contrast, at Ω_2 the wave packet is spreading in both directions [see Fig. 5(b), bottom] and in Fourier space [see Fig. 5(c),

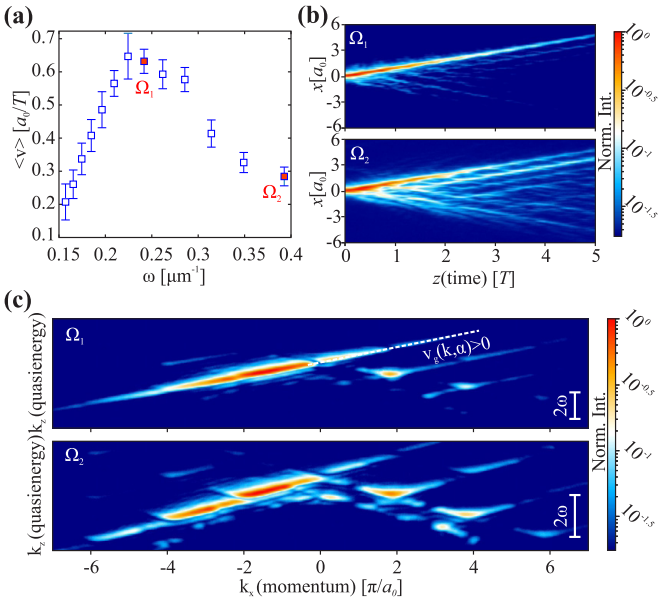

FIG. 5. (a) Measured mean group velocity of a wave packet vs driving frequency ω for the single-site excitation at the input A. (b) Real-space SPP intensity distributions corresponding to the arrays modulated with frequency $\Omega_1 = 0.23\,\mu\text{m}^{-1}$ and $\Omega_2 = 0.39\,\mu\text{m}^{-1}$. (c) Fourier-space SPP intensity distributions for the same arrays as in panel (b).

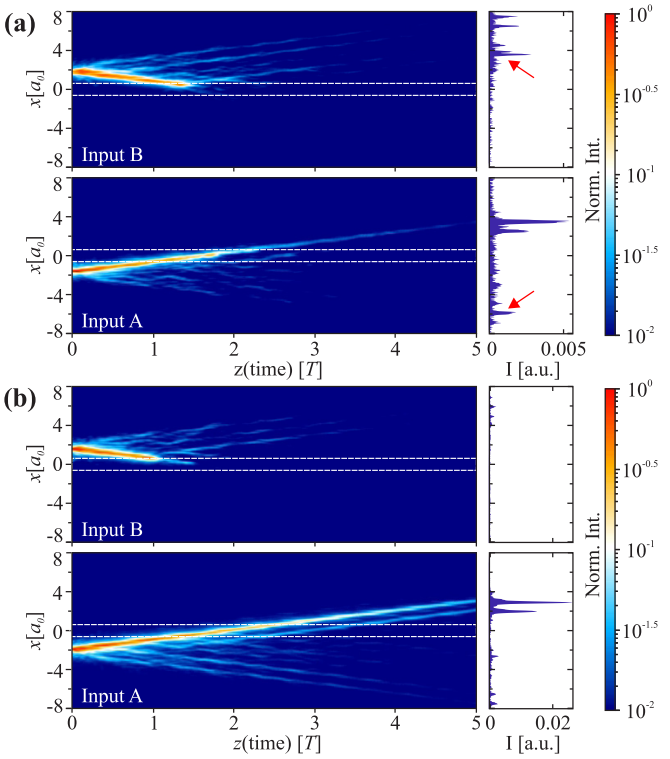

FIG. 6. Real space intensity distributions for the DLSPPW arrays with local modulated dissipation (highlighted by white dashed lines) featuring unidirectional transmittance at Ω_1. The wave packet is excited at $x > 0$ (input B, top) or at $x < 0$ (input A, bottom). The area plots at the right side from the real-space data show the intensity distribution after the propagation distance $z = 5T$. (a) Chromium stripes with $L = 0.3T$ were deposited below two waveguides. The red arrows point to reflected wave. (b) The same as in panel (a), but the length of the Cr stripe was reduced to $L = 0.15T$.

bottom] the gaps between the quasienergy bands broaden, and the states with $v^{\text{g}}_{\alpha,k} < 0$ become noticeably populated. Such a behavior results from hybridization of counterpropagating states and is fully consistent with the theory [compare with Fig. 2(b)].

Next, we fabricate DLSPPW arrays with local modulated losses using the optimal driving frequency Ω_1 determined above. For that, we deposit Cr stripes of length $L = 0.3T$ beneath the two waveguides in between the inputs A and B, so that the phase shift in Eq. (6) is zero $\varphi = 0$ [see Fig. 2(b)]. The inputs are placed such that the excited wave packet impinges upon the region of modulated losses from both sides. In Fig. 6(a), the resulting real-space intensity distributions of SPPs for two input conditions are displayed. Here, the wave packet impinging from the region $x > 0$ (top image) is strongly damped such that no SPPs are visible after the lossy region. Since the transmitted wave is lower than the noise level, the transmission coefficient must be $T_{\alpha=2} < 10^{-2}$. In contrast, when the wave packet impinges from the opposite side, $x < 0$, it is partially transmitted (bottom image). By comparing to the case with no loss, we can estimate the transmission coefficient $T_{\alpha=1} \approx 0.53$. Additionally, the weak reflection from the interface is observed for both sides (see red arrows). This can be related to the slight shift of the Cr stripes in respect to the waveguides, which leads to a nonzero phase shift φ.

We now aim to improve the performance of the direction-dependent filtering in our system; in particular, we want to increase the transmission in the low-loss direction $T_{\alpha=1}$ while keeping the $T_{\alpha=2}$ below the detection limit of $\approx 10^{-2}$. Relying on the numerical calculations discussed above, at the constant loss strength γ_0 this can be realized by reducing the Cr stripe length L. Indeed, for $L = 0.15T$ [Fig. 6(b)], we again observe strong absorption in $-x$ direction such that $T_{\alpha=2} < 10^{-2}$; however, the transmission in the opposite direction is substantially increased $T_{\alpha=1} \approx 0.92$. In this case, we see no reflection from the interface.

VI. CONCLUSION

In conclusion, we proposed and experimentally realized a direction-dependent filter in a Hamiltonian quantum ratchet. Our ratchet scheme on a 1D periodically driven lattice is inspired by the arrays of evanescently coupled waveguides as experimental platform. Using Floquet-Bloch theory, we show that at certain frequencies such a model supports directional transport characterized by helical Floquet bands with negligible dispersion. Based on the sublattice oscillation of the Floquet-Bloch states, we introduce local periodic losses as a method for direction-dependent filtering. In doing so, we achieve strong nonreciprocal transport at all quasimomenta and a vast range of system parameters. In order to quantify nonreciprocal transmission, we develop the Floquet scattering theory for the conceptually interesting though commonly undiscussed case where both bulk and scattering potentials are modulated time periodically. Using this approach, we

calculate asymmetric transmission and reflection coefficients for various system parameters and determine the optimal conditions for direction-dependent filtering. Based on the theoretical predictions, we realize our ratchet model in arrays of coupled periodically modulated plasmonic waveguides. Using real- and Fourier space measurements, we determine the resonant modulation frequency corresponding to the highest group velocity and almost dispersionless bands. Next, the non-Hermitian impurity is implemented by means of an absorber deposited locally below the waveguides in a two-step lithographic process. Nonreciprocal transmission through this impurity is clearly demonstrated by real-space intensity distributions. Our results indicate that it is possible to create a Hamiltonian ratchet being intrinsically nonreciprocal such that any mixed initial state can be filtered to achieve motion in only one chosen direction. Contrary to nonreciprocal transport induced by non-Hermitian gauge fields, no additional gain is needed [42]. This makes our method favourable in further experimental settings such as ultracold quantum gases [13,18].

ACKNOWLEDGMENTS

We acknowledge financial support by the Deutsche Forschungsgemeinschaft through CRC/TR 185 (277625399) OSCAR (C.D., S.E., Z.F., J.K., S.L., A.S.) and through the Cluster of Excellence ML4Q (90534769) (Z.F., J.K., S.L., A.S.).

Z.F. and C.D. contributed equally to this work. Z.F. fabricated the samples, conducted the experiments, contributed to the theoretical understanding of the effects, and prepared the figures. C.D. analyzed the system theoretically, developed the numerical method based on the Floquet S matrix theory, and performed calculations of the transmission and reflection coefficients. Z.F. and C.D. wrote the first draft of the manuscript. A.S. contributed to the theoretical understanding of the ratchet effect and calculated the Floquet spectrum. S.L. conceived the plasmonic experiment and supervised Z.F. and A.S. S.E. and J.K. conceived the theoretical analysis. S.E. supervised C.D. and Z.F., and J.K. supervised Z.F. S.L., S.E., and J.K. contributed to the manuscript writing. All authors discussed the results and reviewed the manuscript.

APPENDIX A: FLOQUET-BLOCH THEORY FOR THE HAMILTONIAN RATCHET

We study our ratchet model within a framework of the Floquet-Bloch theory [34]. For that, we first transform the bulk Hamiltonian from Eq. (1) to k space:

$$H_{\mathrm{Bulk}}(t) = \sum_k \psi_k^\dagger H_k(t) \psi_k. \tag{A1}$$

Here, we introduced $\psi_k = \frac{1}{\sqrt{N_0}} \sum_j e^{-ika_0 j} (c_{j,\mathrm{A}}, e^{-ika_0/2} c_{j,\mathrm{B}})^T$ with the length of the unit cell a_0 and the number of unit cells N_0. The time-dependent Bloch Hamiltonian $H_k(t)$ of our model reads

$$H_k(t) = \begin{pmatrix} 0 & h(k,t) \\ h^*(k,t) & 0 \end{pmatrix}, \tag{A2}$$

where $h(k,t) = J_1(t) e^{ika_0/2} + J_2(t) e^{-ika_0/2}$ and * denotes the complex conjugation. The steady states of the Hamiltonian (A2) are the so called Floquet-Bloch states [34]

$$|\psi_{k,\alpha}(t)\rangle = e^{-i\epsilon_{k,\alpha,m} t} |\phi_{k,\alpha,m}(t)\rangle, \tag{A3}$$

which are composed of a phase factor involving the quasienergy $\epsilon_{k,\alpha,m}$ and the T-periodic Floquet mode $|\phi_{k,\alpha,m}(t)\rangle$. The index m arises from periodicity of the quasienergies, namely $\epsilon_{k,\alpha,m} = \epsilon_{k,\alpha,0} + m\omega$, where $\epsilon_{k,\alpha,0}$ lies in the so-called first Floquet-Brillouin zone $[-\omega/2, \omega/2)$. As the corresponding modes only differ by a phase factor, $|\phi_{k,\alpha,m}(t)\rangle = e^{im\omega t} |\phi_{k,\alpha,0}(t)\rangle$, the solutions from different Floquet-Brillouin zones describe the same physics. In our case, the states can be labeled by their quasimomentum k, the band $\alpha = 1, 2$, and the Floquet index m. The Floquet modes are eigenstates of the Floquet operator $\mathcal{H}_k(t) = H_k(t) - i\frac{\partial}{\partial t}$ in Floquet space $\mathcal{F} = \mathcal{R} \otimes \mathcal{T}$, which consists of the configuration space $\mathcal{R}$ and the space of the time-periodic functions $\mathcal{T}$ [43,44]. This eigenvalue equation reads

$$\hat{\mathcal{H}}_k |\phi_{k,\alpha,m}\rangle\rangle = \epsilon_{k,\alpha,m} |\phi_{k,\alpha,m}\rangle\rangle. \tag{A4}$$

Here $|\phi\rangle\rangle$ is the element of $\mathcal{F}$ which corresponds to $|\phi(t)\rangle$ and $\hat{A}$ is the operator which is acting in $\mathcal{F}$ connected with $A(t)$. When we introduce the Fourier basis $|n\rangle \in \mathcal{T}$ and express $|n(t)\rangle = e^{-in\omega t}$, where $|\phi_{k,\alpha,m}(t)\rangle$ and $H_k(t)$ are written by their Fourier coefficients $f^{(n)} = 1/T \int_0^T dt\, e^{in\omega t} f(t)$, Eq. (A4) transforms to

$$\sum_l \left[H_k^{(n-l)} - n\omega \delta_{n,l} \right] \left| \phi_{k,\alpha,m}^{(l)} \right\rangle = \epsilon_{k,\alpha,m} \left| \phi_{k,\alpha,m}^{(n)} \right\rangle. \tag{A5}$$

Equation (A5) is first truncated in Floquet space by introducing a cutoff such that $|\phi_{k,\alpha,m}^{(n)}\rangle = 0$ for $|n| > m_{\mathrm{cutoff}}$. The resulting eigenvalue problem involving a finite matrix is solved numerically with a cutoff m_{cutoff} large enough to guarantee that the solution has converged.

APPENDIX B: DISCONNECTED DIMER MODEL

In order to qualitatively understand the origin of the rectified transport, we consider the Hamiltonian (2) with a simplified driving scheme, where one period, for $0 \leqslant t < T$, reads

$$J_1(t) = \begin{cases} J, & t \in [t_1, t_1 + \delta t[\\ 0, & \text{otherwise} \end{cases}, \tag{B1a}$$

$$J_2(t) = \begin{cases} J, & t \in [t_2, t_2 + \delta t[\\ 0, & \text{otherwise} \end{cases}. \tag{B1b}$$

Here $t_1 + \delta t < T/2$ with $\delta t > 0$ and $t_2 = T/2 + t_1$. The Schrödinger equation for $|\psi(t)\rangle = \sum_j (\psi_j^{\mathrm{A}} c_{j,\mathrm{A}}^\dagger + \psi_j^{\mathrm{B}} c_{j,\mathrm{B}}^\dagger)|0\rangle$ reads

$$i\partial_t \psi_j^{\mathrm{A}} = J_1(t) \psi_j^{\mathrm{B}} + J_2(t) \psi_{j-1}^{\mathrm{B}}, \tag{B2a}$$

$$i\partial_t \psi_j^{\mathrm{B}} = J_1(t) \psi_j^{\mathrm{A}} + J_2(t) \psi_{j+1}^{\mathrm{A}}, \tag{B2b}$$

where we assume as initial conditions $\psi_j^\gamma(t=0) = \delta_{\gamma,\mathrm{A}} \delta_{j,l}$. For $t \in [0, t_1[$ all couplings are zero and the wave function stays at its initial value. In the interval $t \in [t_1, t_1 + \delta t[$ the state undergoes Rabi oscillations between

sublattices A and B,

$$\psi_l^{\mathrm{A}}(t) = \cos[J(t-t_1)], \tag{B3a}$$

$$\psi_l^{\mathrm{B}}(t) = -i\sin[J(t-t_1)]. \tag{B3b}$$

We assume in the following that population is fully transferred between the sublattices, i.e., the condition $J\delta t = \frac{\pi}{2} + n\pi$ holds with $n \in \mathbb{N}_0$. A similar analysis for the second half of the cycle (B1) yields that the state moves in one driving period T one unit cell to the right $\psi_j^{\gamma}(t=T) = \delta_{\gamma,\mathrm{A}}\delta_{j,l+1}$, while a state starting on sublattice B moves the same length to the left. Thus we created a simple scheme for ideal, rectified transport. The quasienergy bands are linear $\epsilon_{k,\alpha,m} = (-1)^{\alpha-1}(\frac{\omega k}{2\pi} - \frac{\omega}{2}) + m\omega$. Using $\delta t = \delta\xi\, 2\pi/\omega$, we find the driving frequencies where perfect linear bands occur to be

$$\omega_n = \frac{4J\delta\xi}{1+2n}, n \in \mathbb{N}_0. \tag{B4}$$

As Eq. (B4) only depends on the area $J\delta\xi$, it can be generalized to Eq. (3). Also, in this model unidirectional transport can be investigated when an impurity is added. We therefore look at a special scheme for the dissipative impurity potential Eq. (5b):

$$\gamma_{\mathrm{A}}(t) = \begin{cases} \gamma_0, & t \in [t_1+\delta t, t_2[\\ 0, & \text{otherwise} \end{cases}, \tag{B5a}$$

$$\gamma_{\mathrm{B}}(t) = \begin{cases} \gamma_0, & t \in [0, t_1[\cup[t_2+\delta t, T[\\ 0, & \text{otherwise} \end{cases}. \tag{B5b}$$

The right-moving state can transmit unaffected through the impurity, while the left moving state is exponentially damped. The transmission coefficients read

$$T_{\alpha=1} = 1, \tag{B6a}$$

$$T_{\alpha=2} = \exp[-2\gamma_0 L_{\mathrm{DD}}], \tag{B6b}$$

where $L_{\mathrm{DD}} = T - 2\delta t$.

APPENDIX C: FLOQUET SCATTERING THEORY

We are interested in the scattering properties of the Floquet-Bloch states $|\phi_{k,\alpha,m}\rangle\rangle$ in the presence of an in general non-Hermitian impurity operator $V(t)$. In contrast to the common literature [30–33,45], we look at a setup where both bulk and scattering potential are modulated time periodically with the same frequency ω. It turns out that the Lippmann-Schwinger equation for Floquet systems equals a static Lippmann-Schwinger theory in the Floquet space $\mathcal{F}$. It is central to calculate the matrix elements of the Floquet S matrix in the Floquet-Bloch basis $S_{(q,\beta,n),(k,\alpha,m)}$. For a general operator $A(t)$, these matrix elements are defined by $A_{(q,\beta,n),(k,\alpha,m)} = \frac{1}{T}\int_0^T dt\,\langle\phi_{q,\beta,n}(t)|A(t)|\phi_{k,\alpha,m}(t)\rangle$, where the states $|\phi_{k,\alpha,m}(t)\rangle$ are calculated by (A4). The matrix elements of the Floquet S matrix describe the amplitude for finding a particle in the state (q,β,n) after the scattering process if initially it was in state (k,α,m). The Floquet S matrix can be termed as

$$S_{(q,\beta,n),(k,\alpha,m)} = \delta(k-q)\delta_{\alpha,\beta}\delta_{n,m} - 2\pi i\delta(\epsilon_{q,\beta,n} - \epsilon_{k,\alpha,m})T_{(q,\beta,n),(k,\alpha,m)}, \tag{C1}$$

where we introduce the matrix elements of the Floquet T matrix $\hat{T} = \hat{V}\hat{\Omega}^+$, with the impurity operator $\hat{V} \in \mathcal{F}$ and the Møller operator $\hat{\Omega}^+ = \mathbb{I} + (\epsilon + i0^+ - \hat{\mathcal{H}}_{\mathrm{bulk}} - \hat{V})^{-1}\hat{V}$. The matrix elements of the Floquet T matrix are given by the self-consistency equation

$$T_{(q,\beta,n),(k,\alpha,m)} = V_{(q,\beta,n),(k,\alpha,m)} + \sum_{\delta,l}\int_{-\pi}^{\pi} dp \frac{V_{(q,\beta,n),(p,\delta,l)}}{\epsilon_{k,\alpha,m} - \epsilon_{p,\delta,l} + i0^+} T_{(p,\delta,l),(k,\alpha,m)}. \tag{C2}$$

We transform Eq. (C2) to a linear system which is solved numerically by discretizing the quasimomentum space and by introducing a cuttoff $m_{\max}$ in the Floquet index. In our case, where bulk and scattering potential are driven by the same frequency, Eq. (C1) dictates that the scattered waves reside in the same Floquet-Brillouin zone as the incoming wave, while all other channels host evanescent waves. Thus, only a 2×2 submatrix

$$\tilde{S}_{\mathrm{scatt}}(k) = \begin{pmatrix} t_{k,\alpha=1} & r_{-k,\alpha=2} \\ r_{k,\alpha=1} & t_{-k,\alpha=2} \end{pmatrix} \tag{C3}$$

of the Floquet S matrix will be nonzero and contribute to scattering. Here we introduced the k-dependent transmission amplitude $t_{k,\alpha} = 1 - \frac{2\pi i}{|v^g_{\alpha,k}|}T_{(k,\alpha,m),(k,\alpha,m)}$ and reflection amplitude $r_{k,\alpha} = -\frac{2\pi i}{|v^g_{\alpha,k}|}T_{(-k,\beta\neq\alpha,m),(k,\alpha,m)}$ by the nonsingular parts of the Floquet S matrix. The k-dependent transmission and reflection coefficients measuring the probability for these events are given by $T_{k,\alpha} = |t_{k,\alpha}|^2$ and $R_{k,\alpha} = |r_{k,\alpha}|^2$. In our setting, we average these quantities over a full band

$$T_\alpha = \frac{1}{2\pi}\int_0^{2\pi} dk T_{k,\alpha}, \tag{C4a}$$

$$R_\alpha = \frac{1}{2\pi}\int_0^{2\pi} dk R_{k,\alpha}. \tag{C4b}$$

In the case of a Hermitian impurity, the matrix $\tilde{S}_{\mathrm{scatt}}(k)$ is a unitary matrix [30], implying the relation $T_{k,\alpha=1} = T_{-k,\alpha=2}$. This results in equal averages $T_{\alpha=1} = T_{\alpha=2}$ and shows that nonreciprocal transport is not possible in the Hermitian case.

APPENDIX D: SAMPLE FABRICATION

The DLSPPW arrays with locally modulated dissipation are fabricated with a two-step electron beam lithography process (EBL). The sample preparation starts with evaporation of 62 nm of Ag and 2 nm of Cu for adhesion on a cleaned surface of a glass substrate. Then the sample is spin coated with the polymeric resist poly(methyl methacrylate) (PMMA). In the first EBL step, we utilize PMMA as a positive-tone resist in order to fabricate a template for the lossy regions and alignment markers. The areas exposed to the electron beam are dissolved in a developer and 15 nm of Cr is evaporated on top of the substrate. After the lift-off process, we end up with the Cr stripes and the alignment markers at the predefined positions. The width of each Cr stripe is set to 1.3 μm. Then the sample is again spin coated with PMMA and the second

EBL step takes place. Now we fabricate the DLSPPW arrays on top of the Cr stripes using the markers for the alignment. In this step, PMMA acts as a negative tone resist which is achieved by increasing the applied electron dose [46]. Finally, the samples are developed in acetone. The atomic force microscopy measurements revealed that the applied electron dose results in the mean waveguide height of 90 nm and the width of 270 nm, which allows us to work in a single-mode regime at a vacuum wavelength of $\lambda = 0.98\,\mu$m. For these geometrical parameters, the propagation constant of the guided mode is $\beta = \beta' - i\beta'' = \text{const}$, $\beta' = 6.55\,\mu\text{m}^{-1}$ (obtained by numerical simulations with COMSOL MULTIPHYSICS) and $\beta'' = (7.3 \pm 0.02) \times 10^{-3}\,\mu\text{m}^{-1}$ (obtained by measuring propagation length of SPPs). The distance between the adjacent waveguides varies as $d_{1,2} = (2 \pm 0.65 \sin \omega z)\mu$m, $\omega = 2\pi/T$. As shown in Fig. 4(b), the modulated part of the array is preceded by a short straight interval of the length $6\,\mu$m. This region contains the grating coupler (red box) which is used for SPP excitation. The grating is deposited only onto the two waveguides at the left and right sides from the dissipative region (inputs A and B), while the extension of others to this region is needed to prevent fire-end excitation of the adjacent waveguides.

APPENDIX E: LEAKAGE RADIATION MICROSCOPY

SPPs are excited by focusing a TM-polarized laser beam with $\lambda_0 = 980$ nm [numerical aperture (NA) of the focusing objective is 0.4] onto the grating coupler deposited on top of the chosen waveguide. The propagation of SPPs in the array is monitored by real- and Fourier-space leakage radiation microscopy (LRM) [20,39]. The leakage radiation as well as the transmitted laser beam are both collected by a high NA oil immersion objective (Nikon 1.4 NA, 60× Plan-Apo). The transmitted laser was filtered out by placing a knife edge at the intermediate back focal plane (BFP) of the oil immersion objective. The remaining radiation was imaged onto an scientific complementary metal-oxide semiconductor camera (Andor Marana). Real-space SPP intensity distributions were recorded at the real image plane while the momentum-space intensity distribution was obtained by imaging the BFP of the oil immersion objective.

[1] S. Denisov, S. Flach, and P. Hänggi, Tunable transport with broken space-time symmetries, Phys. Rep. **538**, 77 (2014).

[2] M. Smoluchowski, Experimentell nachweisbare, der üblichen Thermodynamik widersprechende Molekularphänomene, Pisma Mariana Smoluchowskiego **2**, 226 (1927).

[3] R. Feynman, R. Leighton, and M. Sands, *The Feynman Lectures on Physics* (Addison Wesley, Reading, MA, 1963), Vol. 1.

[4] G. Mahmud, C. J. Campbell, K. J. Bishop, Y. A. Komarova, O. Chaga, S. Soh, S. Huda, K. Kandere-Grzybowska, and B. A. Grzybowski, Directing cell motions on micropatterned ratchets, Nat. Phys. **5**, 606 (2009).

[5] V. Serreli, C.-F. Lee, E. R. Kay, and D. A. Leigh, A molecular information ratchet, Nature (London) **445**, 523 (2007).

[6] H. Linke, T. Humphrey, A. Löfgren, A. Sushkov, R. Newbury, R. Taylor, and P. Omling, Experimental tunneling ratchets, Science **286**, 2314 (1999).

[7] M. V. Costache and S. O. Valenzuela, Experimental spin ratchet, Science **330**, 1645 (2010).

[8] C. Drexler, S. Tarasenko, P. Olbrich, J. Karch, M. Hirmer, F. Müller, M. Gmitra, J. Fabian, R. Yakimova, S. Lara-Avila *et al.*, Magnetic quantum ratchet effect in graphene, Nat. Nanotechnol. **8**, 104 (2013).

[9] J. Lehmann, S. Kohler, P. Hänggi, and A. Nitzan, Molecular Wires Acting as Coherent Quantum Ratchets, Phys. Rev. Lett. **88**, 228305 (2002).

[10] C. Zhang, C.-F. Li, and G.-C. Guo, Experimental demonstration of photonic quantum ratchet, Sci. Bull. **60**, 249 (2015).

[11] F. Dreisow, Y. V. Kartashov, M. Heinrich, V. A. Vysloukh, A. Tünnermann, S. Nolte, L. Torner, S. Longhi, and A. Szameit, Spatial light rectification in an optical waveguide lattice, EPL **101**, 44002 (2013).

[12] T. Salger, S. Kling, T. Hecking, C. Geckeler, L. Morales-Molina, and M. Weitz, Directed transport of atoms in a Hamiltonian quantum ratchet, Science **326**, 1241 (2009).

[13] J. Ni, S. Dadras, W. K. Lam, R. K. Shrestha, M. Sadgrove, S. Wimberger, and G. S. Summy, Hamiltonian ratchets with ultracold atoms, Ann. Phys. **529**, 1600335 (2017).

[14] P. Hänggi and F. Marchesoni, Artificial Brownian motors: Controlling transport on the nanoscale, Rev. Mod. Phys. **81**, 387 (2009).

[15] P. Reimann, M. Grifoni, and P. Hänggi, Quantum Ratchets, Phys. Rev. Lett. **79**, 10 (1997).

[16] G. G. Carlo, G. Benenti, G. Casati, and D. L. Shepelyansky, Quantum Ratchets in Dissipative Chaotic Systems, Phys. Rev. Lett. **94**, 164101 (2005).

[17] D. J. Thouless, Quantization of particle transport, Phys. Rev. B **27**, 6083 (1983).

[18] S. Denisov, L. Morales-Molina, S. Flach, and P. Hänggi, Periodically driven quantum ratchets: Symmetries and resonances, Phys. Rev. A **75**, 063424 (2007).

[19] J. Gong, D. Poletti, and P. Hanggi, Dissipationless directed transport in rocked single-band quantum dynamics, Phys. Rev. A **75**, 033602 (2007).

[20] Z. Fedorova, H. Qiu, S. Linden, and J. Kroha, Observation of topological transport quantization by dissipation in fast Thouless pumps, Nat. Commun. **11**, 3758 (2020).

[21] M. Lohse, C. Schweizer, O. Zilberberg, M. Aidelsburger, and I. Bloch, A Thouless quantum pump with ultracold bosonic atoms in an optical superlattice, Nat. Phys. **12**, 350 (2016).

[22] S. Nakajima, T. Tomita, S. Taie, T. Ichinose, H. Ozawa, L. Wang, M. Troyer, and Y. Takahashi, Topological Thouless pumping of ultracold fermions, Nat. Phys. **12**, 296 (2016).

[23] B. Höckendorf, A. Alvermann, and H. Fehske, Topological origin of quantized transport in non-Hermitian Floquet chains, Phys. Rev. Res. **2**, 023235 (2020).

[24] W. P. Su, J. R. Schrieffer, and A. J. Heeger, Solitons in Polyacetylene, Phys. Rev. Lett. **42**, 1698 (1979).

[25] Y. V. Kartashov, V. A. Vysloukh, V. V. Konotop, and L. Torner, Diffraction control in PT-symmetric photonic lattices: From beam rectification to dynamic localization, Phys. Rev. A **93**, 013841 (2016).

[26] J. C. Budich, Y. Hu, and P. Zoller, Helical Floquet Channels in 1D Lattices, Phys. Rev. Lett. **118**, 105302 (2017).

[27] D. Thuberg, E. Muñoz, S. Eggert, and S. A. Reyes, Perfect Spin Filter by Periodic Drive of a Ferromagnetic Quantum Barrier, Phys. Rev. Lett. **119**, 267701 (2017).

[28] S. A. Reyes, D. Thuberg, D. Pérez, C. Dauer, and S. Eggert, Transport through an ac-driven impurity: Fano interference and bound states in the continuum, New J. Phys. **19**, 043029 (2017).

[29] A. Agarwala and D. Sen, Effects of local periodic driving on transport and generation of bound states, Phys. Rev. B **96**, 104309 (2017).

[30] M. Moskalets and M. Büttiker, Floquet scattering theory of quantum pumps, Phys. Rev. B **66**, 205320 (2002).

[31] H. Li, B. Shapiro, and T. Kottos, Floquet scattering theory based on effective Hamiltonians of driven systems, Phys. Rev. B **98**, 121101(R) (2018).

[32] D. H. Smith, Inducing Resonant Interactions in Ultracold Atoms with a Modulated Magnetic Field, Phys. Rev. Lett **115**, 193002 (2015).

[33] T. Millack, T-matrix and k-matrix Floquet theory for atoms in strong laser fields, J. Phys. B: At., Mol. Opt. Phys. **23**, 1693 (1990).

[34] A. Gómez-León and G. Platero, Floquet-Bloch Theory and Topology in Periodically Driven Lattices, Phys. Rev. Lett. **110**, 200403 (2013).

[35] A. Guo, G. J. Salamo, D. Duchesne, R. Morandotti, M. Volatier-Ravat, V. Aimez, G. A. Siviloglou, and D. N. Christodoulides, Observation of PT-Symmetry Breaking in Complex Optical Potentials, Phys. Rev. Lett. **103**, 093902 (2009).

[36] W. Song, W. Sun, C. Chen, Q. Song, S. Xiao, S. Zhu, and T. Li, Breakup and Recovery of Topological Zero Modes in Finite Non-Hermitian Optical Lattices, Phys. Rev. Lett. **123**, 165701 (2019).

[37] I. L. Garanovich, S. Longhi, A. A. Sukhorukov, and Y. S. Kivshar, Light propagation and localization in modulated photonic lattices and waveguides, Phys. Rep. **518**, 1 (2012).

[38] F. Bleckmann, Z. Cherpakova, S. Linden, and A. Alberti, Spectral imaging of topological edge states in plasmonic waveguide arrays, Phys. Rev. B **96**, 045417 (2017).

[39] Z. Cherpakova, F. Bleckmann, T. Vogler, and S. Linden, Transverse Anderson localization of surface plasmon polaritons, Opt. Lett. **42**, 2165 (2017).

[40] M. C. Rechtsman, J. M. Zeuner, Y. Plotnik, Y. Lumer, D. Podolsky, F. Dreisow, S. Nolte, M. Segev, and A. Szameit, Photonic Floquet topological insulators, Nature (London) **496**, 196 (2013).

[41] Z. Fedorova, C. Jörg, C. Dauer, F. Letscher, M. Fleischhauer, S. Eggert, S. Linden, and G. von Freymann, Limits of topological protection under local periodic driving, Light: Sci. Appl. **8**, 63 (2019).

[42] S. Longhi, D. Gatti, and G. Della Valle, Non-Hermitian transparency and one-way transport in low-dimensional lattices by an imaginary gauge field, Phys. Rev. B **92**, 094204 (2015).

[43] A. Eckardt, Colloquium: Atomic quantum gases in periodically driven optical lattices, Rev. Mod. Phys. **89**, 011004 (2017).

[44] H. Sambe, Steady states and quasienergies of a quantum-mechanical system in an oscillating field, Phys. Rev. A **7**, 2203 (1973).

[45] H. Li, T. Kottos, and B. Shapiro, Floquet-Network Theory of Nonreciprocal Transport, Phys. Rev. Appl. **9**, 044031 (2018).

[46] A. Block, C. Etrich, T. Limboeck, F. Bleckmann, E. Soergel, C. Rockstuhl, and S. Linden, Bloch oscillations in plasmonic waveguide arrays, Nat. Commun. **5**, 3843 (2014).